A fault diagnosis method based on low signal to noise ratio vibration measurement for use in casing cutters

OPEN ACCESS
IOP Publishing
Measurement Science and Technology
Meas. Sci. Technol. **33** (2022) 045102 (12pp)
https://doi.org/10.1088/1361-6501/ac3854

A fault diagnosis method based on low signal to noise ratio vibration measurement for use in casing cutters

Pu Zhang[1], Shuyao Liu[1], Aihua Tao[2], Jingjing Cheng[1,*] and Peng Gao[1]

[1] MOE Key Laboratory of Image Processing and Intelligence Control, School of Artificial Intelligence and Automation, Huazhong University of Science and Technology, Wuhan, People's Republic of China
[2] Well-Tech R&D Institutes, China Oilfield Services Limited, Hebei 065201, People's Republic of China

E-mail: chengjj@hust.edu.cn

Received 19 August 2021, revised 9 October 2021
Accepted for publication 8 November 2021
Published 7 January 2022

Abstract

In this paper, a method for fault diagnosis in casing cutters is proposed. A vibration signal acquisition circuit for use in a high-temperature environment was designed, and a casing cutter measurement model was established, including a model of the casing cutter in a trouble-free state and two other common fault states. The vibration characteristics of the model were analyzed. A fault feature enhancement model based on enhancement of the signal to noise ratio and sparse representation, which effectively solves the fault diagnosis problem caused by the limited installation location and the limited performance of the vibration measurement at high temperature, was also designed. The MobileNet-V3-Small convolutional neural network (CNN) model was improved by reducing the basic blocks of the continuous homogeneous structure in the original model, and the Squeeze and Excitation structure expanded to the global level to obtain a lightweight CNN fault recognition model. The effectiveness and efficiency of the proposed method were validated by various experiments.

Keywords: fault diagnosis, vibration measurement, casing cutter

(Some figures may appear in colour only in the online journal)

1. Introduction

The role of the casing is mainly to protect the wellbore, seal the oil–vapor–water triplex and provide a flow pipeline for downhole fluids [1, 2]. An electric casing cutter is a well repair tool for repairing damaged well casings [3, 4]. Casing cutters are highly susceptible to various failures due to factors such as cutting vibrations, greater rigidity of casing materials and high-temperature and high-pressure logging environments. To ensure the safety of the entire operation and reduce economic losses caused by apparatus failure, casing cutter fault diagnosis based on vibration measurement is necessary [5–7]. Recently, deep learning technology has been widely used in fault identification based on vibration measurement, for example: (a) application of the spectral kurtosis technique to select the frequency bandwidth, which contains the fault characteristics, for fault detection of rolling bearings [8]; (b) a fault diagnosis method based on variational pattern decomposition and an improved convolutional neural network (CNN) [9]; (c) a fault diagnosis method based on multivariate singular spectral decomposition and improved Kolmogorov complexity [10], which has shown good performance in fault diagnosis [11, 12]. However, most studies have focused on how to optimize the model [10–12] and little attention has been paid to two problems caused by the limited mounting position of acceleration

* Author to whom any correspondence should be addressed.

sensors in engineering applications, namely: (a) incomplete observation of the phenomenon [13] and (b) the low signal to noise ratio (SNR) of the acquired acceleration signals [14]. The impact of these problems on machine learning-based fault diagnosis methods has not yet seen much research.

This paper introduces a vibration measurement model and also illustrates the low quality of vibration measurement due to incomplete observation (section 2), designs a data acquisition and processing circuit, verifies its performance under high-temperature conditions (section 3), designs a fault feature enhancement model based on SNR enhancement and sparse representation (section 4) and describes the improved MobileNet-V3-Small method (section 5). Finally, an experimental validation is conducted (section 6) and a summary and outlook given (section 7).

2. Dynamic modeling of a casing cutter

The structure of a high-temperature downhole casing cutter is shown in figure 1, including the connecting head, the hydraulic part, the motor anchoring part and the cutting part. The entire cutting motion is executed in three parts: anchoring, cutter rotation and feed.

Based on the structure and cutting process of a casing cutter, finite element analysis of the vibration characteristics was performed for three cases: trouble-free, anchoring eccentricity failure and severe failure of broken teeth. As shown in figure 2, (a) is a trouble-free state, (b) is anchoring eccentricity failure, in which the center of the apparatus skeleton and the center of the pipe being cut do not coincide, and (c) is a severe failure of broken teeth.

The finite element analysis of the failure model for the three states is shown in figure 3. The relevant conditions are set as follows: cutting blade speed 5000 revolutions per second, connection rod speed 6 revolutions per minute, distance between the acceleration measurement point and skeleton head 4.5 m; the 3D model material property is a rigid alloy. ADAMS software automatically obtains the acceleration signal of the measurement point according to the pre-set vibration condition. The SNR is calculated from the power of the noise signal and the power of the acceleration signal. The SNR of acceleration signals in the three states is −9.657 dB, −14.122 dB and −12.699 dB, respectively.

The continuity of the trouble-free vibration signal in figure 3(a) is excellent, and it can be seen that there is no more obvious jamming during cutting. The anchoring eccentricity fault has a very obvious vibration signal interruption, which is caused by the blade failing to contact the pipe being cut in part of the cutting position after the anchoring eccentricity, as shown in figure 3(b). The blade in figure 3(c) has a severely broken tooth with a large sudden change in vibration signal and low cutting stability.

Due to the distance between the location of the accelerometer installation and the actual vibration point, the acceleration signal acquired by the vibration sensor is attenuated, and the attenuation of high-frequency components is more obvious [15]. In order to more intuitively represent the characteristics

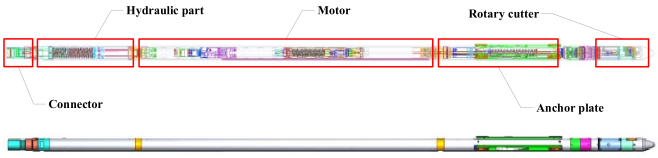

Figure 1. Main structure of a casing cutter.

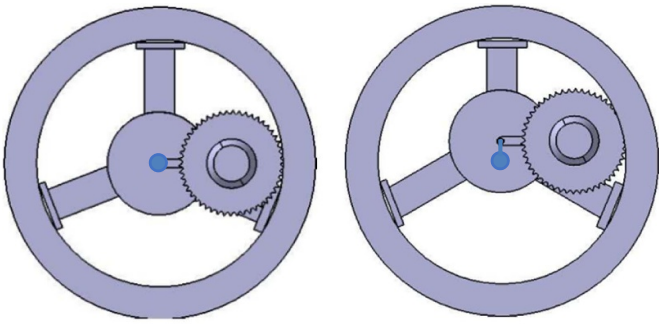

(a)Trouble-free (b)Anchoring eccentricity failure

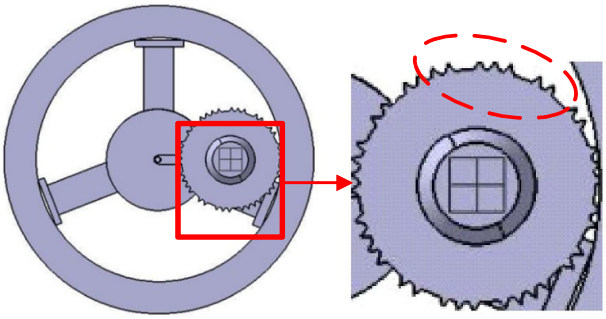

(c)Severe failure of broken teeth

Figure 2. Simplified model of casing cutters.

of the vibration signal, envelope spectrum analysis of the vibration signal was performed in the finite element analysis.

Figure 4 shows the envelope spectra of a trouble-free vibration signal, a vibration signal for a blade with a severe broken tooth fault and an anchoring eccentric vibration fault signal in finite element analysis. From figure 4, it can be seen that it is difficult to distinguish fault states by using the spectrum analysis method directly.

3. The vibration signal acquisition circuit used in a high-temperature environment (HT-VSA)

We designed a HT-VSA. It mainly comprises external axial and radial single-axis accelerometers, a digital signal processor (DSP), a voltage monitoring circuit, a data communication circuit and the corresponding power supply module, as shown in figure 5. Commercial off-the-shelf components are used widely when developing instruments for use in high-temperature environments, but the behavior and high-temperature tolerance of each component needs to be evaluated carefully before it can be used [15]. The measurement circuit of this design operates for a long period of

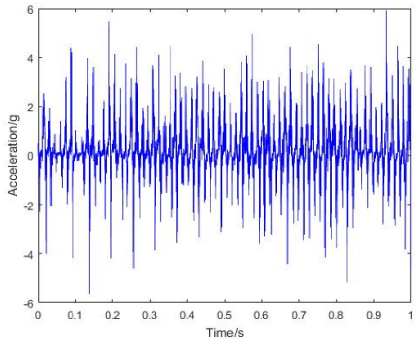

(a) Trouble-free

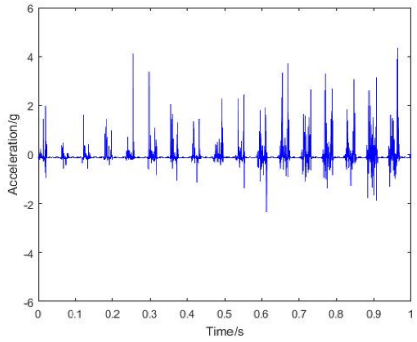

(b) Anchoring eccentricity failure

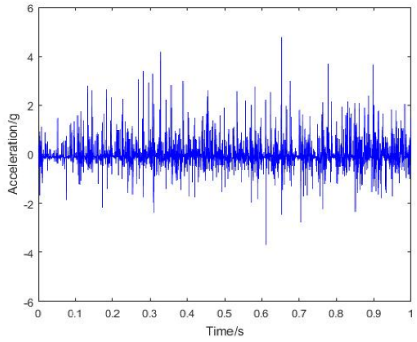

(c) Severe failure of broken teeth

Figure 3. Finite element analysis of vibration signals.

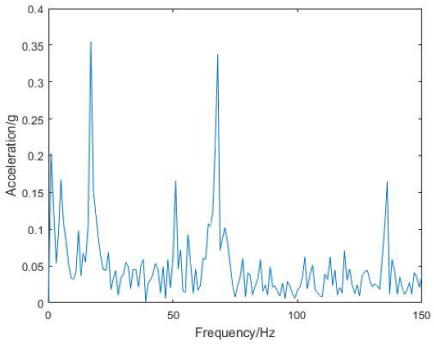

(a) Trouble-free

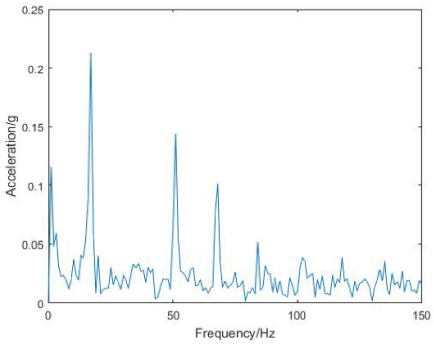

(b) Anchoring eccentricity failure

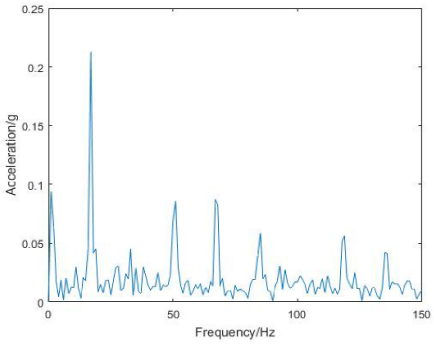

(c) Severe failure of broken teeth

Figure 4. Finite element analysis of the envelope spectrum of vibration signals.

time at 150 °C downhole. Considering the high-temperature environment downhole, each chip used in the module is tested to determine the temperature at which it begins to fail and generate errors associated with thermal damage. For this circuit we selected a TI TMS320F28069 chip as the core processor: this chip is a real-time control MCU with a 32-bit core (C28× CPU) that provides single-cycle operation and speeds up to 300 MIPS, plus a highly optimized peripheral and interrupt management bus, designed for a variety of control applications. In addition, its floating-point unit supports fast multiplication, addition, subtraction, etc. Its triangular nonlinear PID math unit (TMU) supports fast SIN, COS, ATAN, EXP, etc. The selected accelerometer was an Analog Devices (ADI) ADXL1003 accelerometer: this accelerometer is a high-temperature acceleration sensor with a measured operating temperature up to 150 °C, sensitivity up to 9.2 mV g^{-1}, a range of 200 g and a low noise density, suitable for vibration monitoring. In addition, its small size makes it suitable for installation on the instrument skeleton of the high-temperature downhole casing cutters where space is tight. The selected amplifier was an ADI AD822: its operating temperature can reach between 150 °C and 170 °C, the temperature drift of the parametric voltage is as low as 2 °C and it has high-temperature performance to meet the needs of the voltage monitoring circuit. The RS-485 chip was a Texas Instruments SN65HVD11: the SN65HVD11 is a special RS-485 transceiver for high-temperature special environments; its maximum operating temperature can reach 210 °C. In terms of transmission rate, its command rate is 10 Mbps. The differential load capacitance on the bus is 50 and the differential load resistance is 60 Ω for multi-machine communication.

The DSP acts as the master controller and computing unit of the circuit, controlling the other unit circuits to work

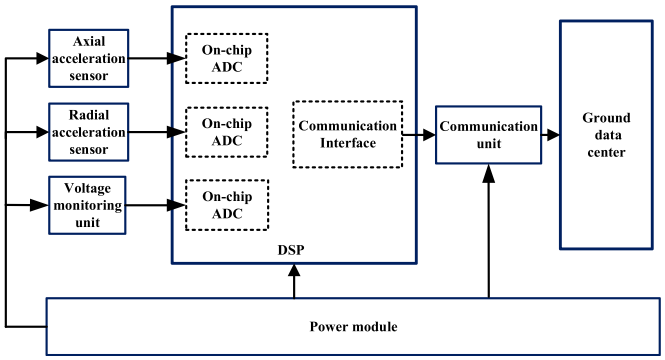

Figure 5. Hardware circuit structure.

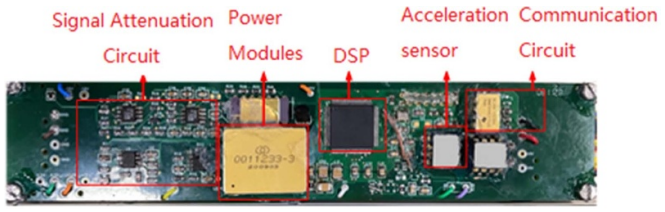

Figure 6. Photograph of the HT-VSA circuit.

together and run the data noise reduction processing algorithm to process the acceleration signal in real time. Axial and radial accelerometers measure the vibration acceleration signal during the operation of the casing cutter. The voltage monitoring circuit is responsible for monitoring whether the supply voltage of the accelerometer is normal or not, to prevent the measurement data from being incorrect due to the abnormal power supply of the accelerometer. The data communication circuit is responsible for packaging and uploading the data to the master systemafter noise reduction processing. A photograph of the circuit is shown in figure 6.

The conversion of the voltage signal output from the accelerometer, i.e. the performance of the ADC in high-temperature environments, determines the quality of the vibration signal measurement. To test the high-temperature quality of the accelerometer voltage monitoring circuit and the analog to digital converter (ADC) of the HT-VSA, a high-temperature linearity test of the voltage monitoring circuit and a high-temperature performance test experiment of the ADC were conducted. Four stable temperature points (25 °C, 100 °C, 125 °C and 175 °C) were selected in the range of 25 °C–175 °C. The first three temperature points were maintained for 30 min each, and the last was maintained for 240 min. The experimental setup is shown in figure 7.

The input signal was a low-distortion sinusoidal signal at 1 kHz and the digitization results were recorded. The following performance parameters used to quantitatively represent the analog-to-digital conversion circuit were calculated: the SINAD (signal to noise and distortion ratio, reflects the cumulative effect of all transfer function

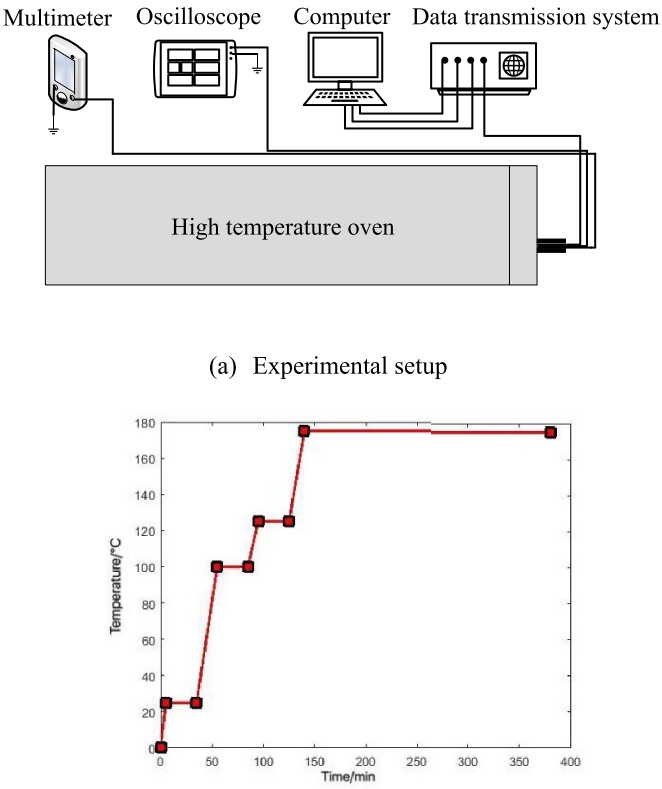

(a) Experimental setup

(b) Temperature setting

Figure 7. Experimental setup for the high-temperature performance test.

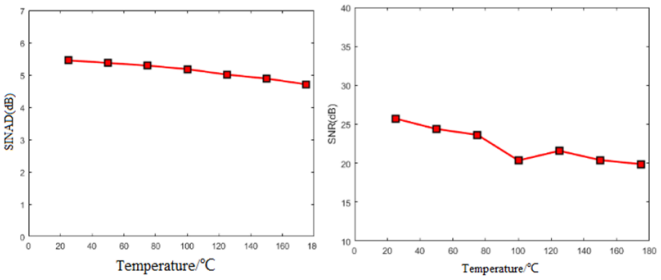

(a)Relationship between SINAD and temperature (b)Relationship between SNR and temperature

Figure 8. The relationship between SINAD, SNR and temperature.

nonlinearities in the output signal and all noise in the system) and the SNR (the ratio of signal energy to quantized noise energy, which can measure the internal noise level of the device). The results produced the curves shown in figure 8.

As shown in figure 8(a), SINAD is 1.373 dB lower at 175 °C than at 25 °C. Figure 8(b) shows that the SNR is 5.847 dB lower at 175 °C than at 25 °C. The reason for this phenomenon is that the thermal noise of the electronic system increases with temperature. As can be seen in figure 8, the SINAD and SNR of the HT-VSA are still within the allowable range at 175 °C, which indicates that the ADC of the HT-VSA has good performance at high temperatures.

4. Design and verification of a fault feature enhancement model based on SNR enhancement and sparse representation

Finite element analysis of the casing cutter model shows that the vibration acceleration data with low SNR have more characteristic harmonics in their envelope spectrogram after the envelope spectrum analysis, and it is difficult to distinguish different fault states by directly using the envelope spectrum analysis method. At the same time, in a real-world application, the signal contains more noise components, resulting in the loss of information containing fault characteristics. To solve the above problems, in this section we design a fault feature enhancement model based on SNR enhancement and sparse representation from the perspective of the discomfort problem and signal recovery, which provides the basis for subsequent classification of casing cutter faults.

4.1. Fault feature enhancement based on SNR enhancement

Assuming that the observed vibration signal is y, the observed signal can be expressed as equation (1), where x is the original signal, H is the degenerate matrix and v is the additive noise

$$y = Hx + v. \tag{1}$$

Assuming that the signal to be recovered is s and the additive observation noise is n. The ultimate goal of the signal recovery process is to solve for a vector $w = [w_1, w_2, w_3, \cdots w_N]^T$, which in turn does the signal recovery. The recovered signal satisfies equation (2), where $\hat{s}$ is an estimate of the original signal s. This process can be expressed as the process of maximizing the SNR, i.e. $\max\text{SNR} = \frac{P_{\hat{s}}}{P_n}$, where $P_{\hat{s}}$ and P_n are the power of the original estimate $\hat{s}$ and additive observation noise n

$$w^T s = \hat{s} + w^T n. \tag{2}$$

The power of the signal can be expressed in terms of its second-order statistics, and then the SNR can be expressed as in equation (3)

$$\text{SNR} = E\left\{\hat{s}(k)\hat{s}(k)^T\right\} \Big/ w^T E\left\{n(k)n(k)^T\right\} w. \tag{3}$$

Assuming $J = E\left\{n(k)n(k)^T\right\} = E\left\{(s(k) - \hat{s}(k))\,(s(k) - \hat{s}(k))^T\right\}$, then the equivariant form of the SNR is as in equation (4)

$$\text{SNR} = E\left\{\hat{s}(k)\hat{s}(k)^T\right\} \Big/ w^T J w. \tag{4}$$

According to equation (4), the maximization SNR problem is equivalent to the minimization J problem. The minimization J problem can be described as follows: based on the observed signal $\{s(1), s(2), s(3), \cdots, s(N)\}$, find the linear minimum variance estimate of the state $s(k)$.

As is well known, the Kalman filtering problem is: find the linear minimum variance estimate $\hat{X}(j|k)$ of state $X(j)$ based on the observed signal $\{Y(1), Y(2), Y(3), \cdots, Y(N)\}$.

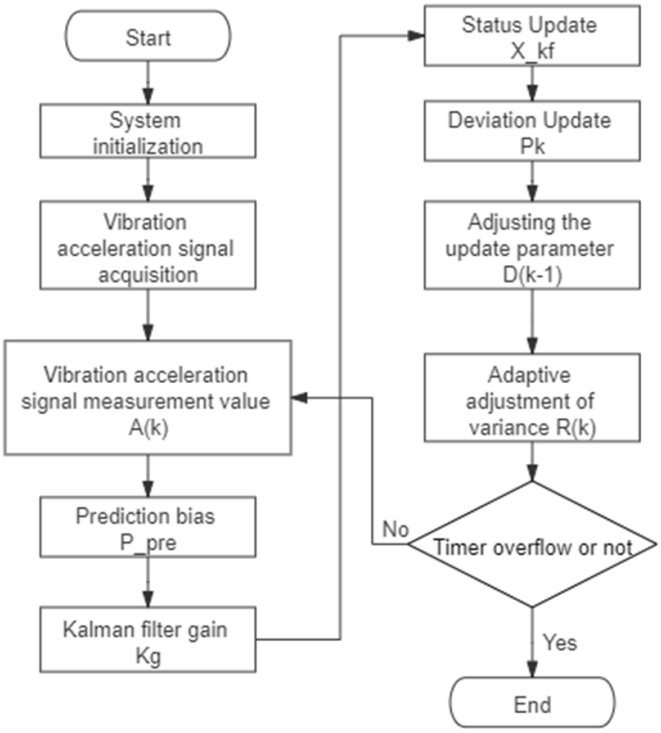

Figure 9. Kalman filtering algorithm flow chart.

The minimization performance index is shown in equation (5)

$$J = E\left[\left(X(j) - \hat{X}(j|k)\right)^T \left(X(j) - \hat{X}(j|k)\right)\right]. \tag{5}$$

It can be seen that the essence of these two problems is the same, so the fault feature enhancement described in this section is implemented based on Kalman filtering. The flow chart of the algorithm is shown in figure 9.

4.2. Fault feature enhancement based on sparse representation

SNR enhancement can greatly weaken the effect of additive noise v and significantly reduce the number of redundant harmonics in the envelope, but what is obtained at this point is not the best estimate of the original signal x. The effect of the degenerate matrix H on the solution of the original signal x still exists. The existence of the degenerate matrix H makes the two almost identical original signals x corresponding to the observed signal y very different, and only by mastering the relevant description and characteristics of the degeneracy matrix H can we solve this problem.

The additive noise v is greatly attenuated by the SNR enhancement, and its residual value is $\dot{v}$. Ideally $\dot{v}$ is small; when $\dot{v}$ can be neglected, the following expression is given:

$$y = Hx. \tag{6}$$

The sparse model considers y as the input to the model, x as the sparse matrix and H as the dictionary. The goal of the

sparse representation is to solve for H under the condition that $\min\|x\|$. Solving H is a nonlinear optimization problem with a mathematical model as in equation (7), where γ is a parameter that balances x_i fidelity and sparsity and takes a value greater than 0 [16]

$$\min_{H,x_i}\sum_{i=1}^{N}\|y_i - Hx_i\|_2^2 + \gamma\sum_{i=1}^{N}\|x_i\|_1. \tag{7}$$

In fact, the computational effort of the dictionary H solution is very large and the properties of H are unknown. The Rudin–Linos–Osher model uses a wavelet basis to make a sparsity constraint on the signal, and this constraint can be expressed as a minimization problem for the energy generalization, with the expression shown in equation (8)

$$E(u) = \int (y/x)^2 dxdy + \|x - Wq\|_2^2 + \tau\|q\|_1 \tag{8}$$

where y is the signal to be recovered, x is the final signal, W is the wavelet basis, q is the sparse representation coefficient of the final signal on the wavelet basis and τ is the regularization coefficient [17]. Wavelet basis is a typical representative of dictionary analysis; the use of wavelet basis as a dictionary basis for sparse representation can both represent the detailed features of the original signal effectively and achieve a simple solution [18, 19]. The reason for this is that, in equation (8), the first fidelity term, the second and third terms are the sparsity constraint terms of the signal to be recovered, which can ensure the sparsity of the signal to be recovered on the wavelet basis; because H does not have sparsity, the interference of H with the recovered signal can be effectively removed by this sparsity constraint.

The vibration signal can be considered as a continuous signal with multiple components, which can be expressed as equation (9) after neglecting the additive observation noise residual v, where $A_i(t)$ and $\omega_i(t)$ denote the instantaneous amplitude and frequency of the ith component of the vibration signal

$$y(t) = \sum_{i=1}^{k} A_i(t)\cos\omega_i(t). \tag{9}$$

The continuous wavelet transform coefficients of $y(t)$ are shown in equation (10), where $\varphi^*(\cdot)$ is the conjugate function of the parent wavelet $\varphi(\cdot)$, and m and n are the wavelet scale and displacement factors

$$W_y(m,n) = m^{-1/2}\int y(t)\,\varphi^*(t - n/m)\,\mathrm{d}t. \tag{10}$$

For any combination of points (m,n), if $W_y(m,n) \neq 0$, the instantaneous frequency f_s can be expressed as equation (11)

$$f_s(m,n) = -i(W_y(m,n))^{-1}\frac{\partial}{\partial n}W_y(m,n). \tag{11}$$

$f_s(m,n)$ constructs the mapping relation from (n,m) to $(n,f_s(m,n))$, and the time–frequency representation can be written as equation (12), where $h(\cdot) \in C_0^\infty$ is a smooth function satisfying $\|h\|_{L^1} = 1$ and δ is the accuracy

$$T_y(f,n) = \int W_y(m,n)\,a^{-3/2}\frac{1}{\delta}h\left(f - f_s(a,b)/\delta\right)\mathrm{d}a. \tag{12}$$

If δ is sufficiently small, it can be seen as a partial inversion of the continuous wavelet transform of f on scale m. In this case, only the small frequency band around the horizontal curve in the timescale plane is preserved, where $f_s(m,n) \approx f$ is preserved and the rest of the plane is ignored. If $\delta \to 0$, then the inverse domain is concentrated on the horizontal curve, i.e. $(m,n) : f_s(m,n) = f$. The above decomposition process of the signal y can obtain the sparse representation $T_y(f,n)$ of the point feature of the original signal, which is a two-dimensional time–frequency vector. This two-dimensional time–frequency vector avoids the complex dictionary H solving process, and thus simplifies the calculation.

5. Improved lightweight CNN

After the feature enhancement process, the obtained images need to be fed into a CNN model for fault type identification. The current problems faced by CNN-based fault identification and classification methods when applied to high-temperature downhole casing cutters are twofold: (a) large CNN models affect the real-time performance of fault identification; (b) insufficient fault data from high-temperature downhole casing cutters. To solve these two problems, this section will improve one kind of lightweight CNN, MobileNet-V3-Small [20, 21], with the aim of reducing the computation of the model and improving its computation speed.

The MobileNet model in the traditional sense first optimizes each basic block by the neural architecture search algorithm to get the general structure of the network, and then designs the specific structure of each layer by the NetAdapt algorithm to determine the number of channels for each filter. The model in this section discards the cumbersome MobileNet model design process and is based on the structure of the MobileNet-V3-Small model, which reduces the number of layers in the model by cutting down the basic blocks of its continuous structure. In addition, the Squeeze and Excitation (SE) structure is extended to the global level to further increase the weight of the effective features [18]. The structure diagram of the improved model is shown in figure 10. The input for the improved model is first computed by the first layer of depth-separable convolution to obtain the first layer output. The first layer output is computed by the basic block of the improved model to obtain the second layer output. The basic blocks of the improved model include standard convolution, depth-separable convolution, the SE module and a summation module, where the two preceding and following standard convolutions and the summation module form a reverse residual structure. The second to eighth layers all use the reverse residual structure and the second to ninth layers all have SE modules. The tenth layer is a pool layer, the eleventh layer is a fully-connected layer and, finally, the twelfth layer outputs identification information.

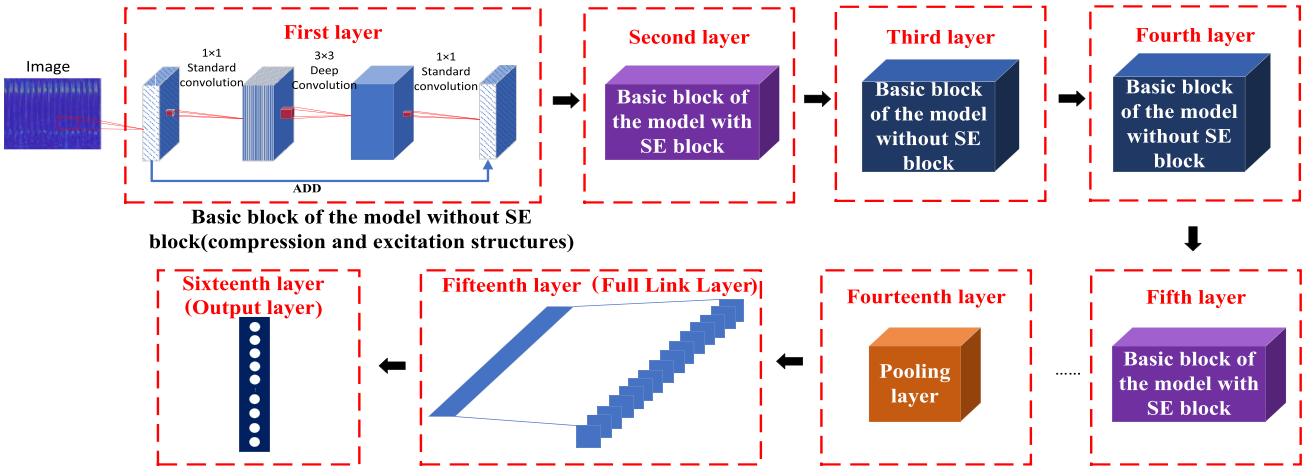

(a) Structure of the model without improvement

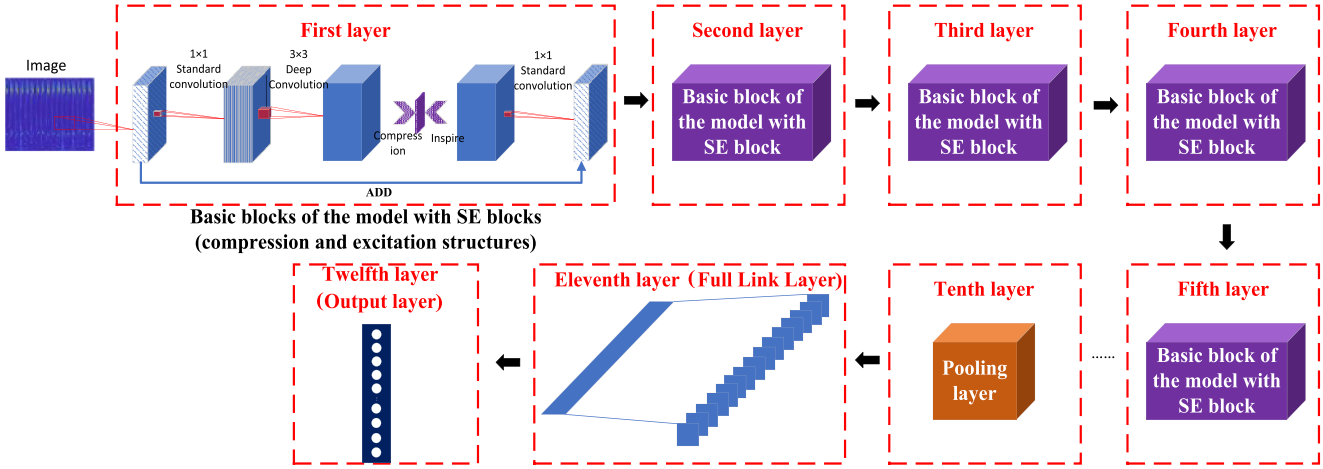

(b)Improved model structure

Figure 10. Structure diagram of the improved MobileNet-V3-Small model.

Table 1. Comparison of original and improved models.

Feature	MobileNet-V3-Small	Improved model
Number of layers	16	12
Layer with SE module	2, 5–13	2–9
Activation function per layer	1, 5–13, 15 are HS	1, 5–9, 11 are HS
	2–4 are RE	2–4 are RE
	13, 15 No activation function	10, 12 No activation function
Steps per level	1–3, 5, 10 steps are 2, the rest are 1	1–3, 5, 8 steps are 2, the rest are 1

HS denotes the H-Swish activation function and RE denotes the ReLU-6 activation function.

A comparison of the structure of the improved model and the original MobileNet-V3-Small model is shown in table 1.

The improved model retains the ReLU-6 activation function from the original basic MobileNet-V3-Small model. The expression of the ReLU-6 activation function is shown in equation (13). From equation (13), the output bound of the ReLU-6 activation function is 6. Compared with the ReLU activation function of equation (14), the ReLU-6 activation function has better robustness, and multiple uses of this activation function can enhance the generalization ability of the model

$$\text{ReLU-6}(n) = \begin{cases} 0 & (n < 0) \\ n & (0 \le n \le 6) \\ 6 & (n \ge 6) \end{cases} \tag{13}$$

$$\text{ReLU}(n) = \begin{cases} 0 & (n \le 0) \\ n & (n > 0). \end{cases} \tag{14}$$

As shown in equation (15), the Swish activation function contains the sigmoid function, which leads to a huge amount of computation, so the original MobileNet-V3-Small model uses the H-Swish activation function. The H-Swish activation

function is an approximate replacement for the Swish function and reduces the computational effort; the improved model also inherits the advantages of this activation function and retains this part. The H-Swish activation function expression is shown in equation (16)

$$\text{Swish}(n) = n \cdot \sigma(n) \tag{15}$$

$$\text{H-Swish}(n) = n \cdot (\text{ReLU-6}(n+3))/6. \tag{16}$$

6. Experimental results

The experimental results illustrate the effectiveness of the methodology of this paper in three ways: (a) analysis of fault characterization results based on SNR enhancement; (b) analysis of fault feature enhancement results based on sparse representation; (c) analysis of recognition results and performance with the improved fault recognition model. All data in the experiments were obtained from the actual operational data of the CNOOC-Oilfield Technology Research Institute cable-type casing cutter platform.

6.1. Analysis of fault feature enhancement results based on SNR enhancement

Fault feature enhancement based on SNR enhancement using actual operational data of high-temperature downhole casing cutters with trouble-free, severe blade tooth breakage and anchoring eccentricity, represented by the time domain signal comparison with and without enhancement, is shown in figure 11. Here the blue curve is the time domain signal plot without SNR enhancement of the vibration signal and the red curve is the time domain signal plot with SNR enhancement. Since SNR enhancement greatly weakens the effect of additive noise, the initial recovered signal amplitude becomes lower.

Figure 12 shows a comparison of the envelope with and without SNR enhancement for each state. The blue curve indicates the signal envelope without SNR enhancement and the orange curve indicates the signal envelope with SNR enhancement. The characteristic harmonic amplitude and the number of effective characteristic harmonics are significantly reduced by SNR enhancement, indicating that fault feature enhancement based on SNR enhancement plays a significant role in fault feature recovery; however, this recovery is not complete, and there are still redundant harmonics in the envelope.

6.2. Analysis of fault feature enhancement results based on sparse representation

The result of the sparsification process is shown in figure 13, with the high-frequency region at the top and the low-frequency region at the bottom of each subplot. Comparing each subplot, it can be seen that the trouble-free case has a higher concentration of data points in both the

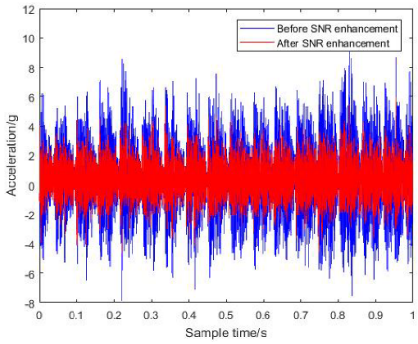

(a) Trouble-free

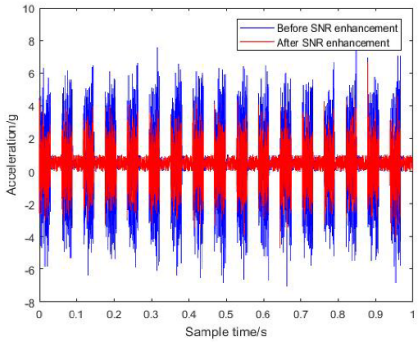

(b) Anchoring eccentricity failure

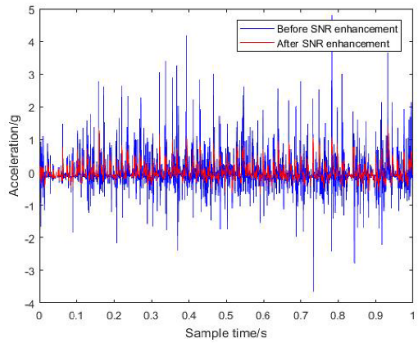

(c) Severe failure of broken teeth

Figure 11. Comparison of vibration signals with and without SNR enhancement.

high-frequency and low-frequency regions compared with the severe blade breakage fault and the anchoring eccentricity fault. However, severe blade breakage faults and anchoring eccentricity faults cannot be accurately identified by the concentration of data points in the high-frequency and low-frequency regions alone.

A comparison of the two-dimensional time–frequency vector sweep region is shown in figure 14. It is evident that the sweeping phenomenon is more pronounced in the sweeping area of the two-dimensional time–frequency vector diagram of the anchoring eccentricity fault compared with the trouble-free case and the severe blade breakage case. In summary, the two-dimensional time–frequency vector diagrams of the three cases are characterized as follows:

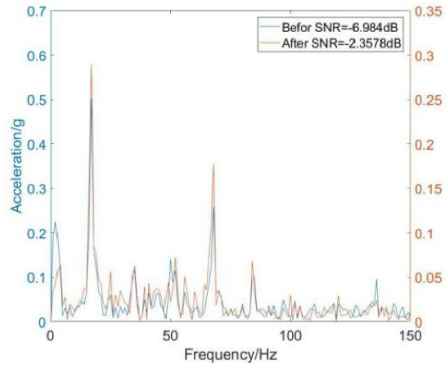

(a) Trouble-free

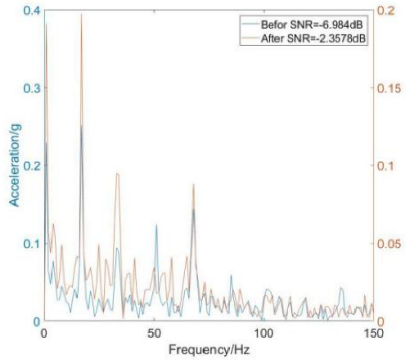

(b) Anchoring eccentricity failure

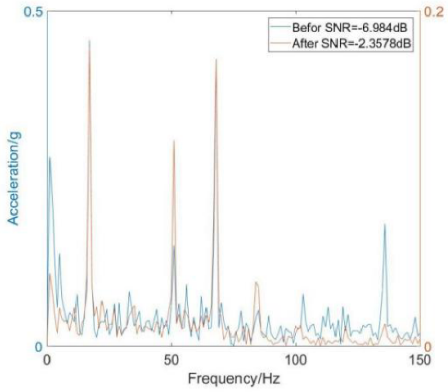

(c) Severe failure of broken teeth

Figure 12. Comparison of envelope spectra with and without SNR enhancement.

(a) trouble-free: data points are concentrated in both the high-frequency and low-frequency regions, with no obvious sweeping;
(b) anchoring eccentricity: data concentration in the high-frequency region and data dispersion in the low-frequency region, without an obvious sweeping phenomenon;
(c) severe failue of broken teeth: the data in the high-frequency region are concentrated and the data in the low-frequency region are scattered, with an obvious sweeping phenomenon.

6.3. Analysis of the recognition results and performance of the improved fault recognition model

6.3.1. Recognition accuracy of the improved model. This section compares the performance of the basic MobileNet-V3-Small model with the improved model under a faulty casing cutter dataset from comparison experiments using enhanced time–frequency vector maps based on the vibration acceleration data features obtained in section 6.2 for thethree states. The numbers are 100 for the no-fault state, 80 for the severe blade breakage state, and 90 for the anchored eccentricity state. In addition, there are 300 time–frequency vector maps in the unlabeled dataset. In real industrial scenarios, the acquisition of fault data (i.e. tagged data) is often extremely difficult, and in many cases no-fault samples are even available. Currently, there are insufficient fault data (labeled data) available for training models for high-temperature downhole casing cutters, and a semi-supervised learning–pseudolabeling model performance enhancement method was used to process the datasets and use them to train MobileNet small convolutional neural network (MN-CNN) models [21–26]. For model training, Softmax was used as the classifier in the output layer, and one-hot encoding was used to encode the three-state categories. The loss function was cross-entropy loss, the optimization algorithm ADAM, the weight decay was set to 1×10^{-3} and the momentum to 0.999. A trend graph of recognition accuracy with the number of training iterations was obtained, and is shown in figure 15. As can be seen from the figure, although the improved model reduces the number of layers in the model by cutting down the basic blocks of the continuous homology structure, the recognition accuracy is relatively high due to the expansion of the squeeze and excitation structure to the global level, which further increases the weight occupied by the effective features.

6.3.2. Impact of epoch on model performance. In this experiment, the learning rate was set to 0.0001, the batch size was 30 and the epoch was changed with a step size of 10 and an initial value of 10 to obtain the experimental results, as shown in figure 16. From the figure, it can be seen that the fault recognition accuracy tends to rise during the iterative training times from 10 to 30; however, when the number of iterations reaches 40, the accuracy fluctuates and then rises back to the highest accuracy. This is due to the fact that the model continues iterative training after training to the highest accuracy, which breaks the original stable structure and affects the stability of the model, resulting in the model no longer being in the best performance state and the accuracy rate drops. After more than 60 iterations this damage will be difficult to recover, and the accuracy of the model will drop linearly.

6.3.3. Impact of learning rate on model performance. In the experimental results in the previous section, the highest accuracy of the network model was obtained when the number of iterations was 30 (or 60) and the batch size was 30. In order to

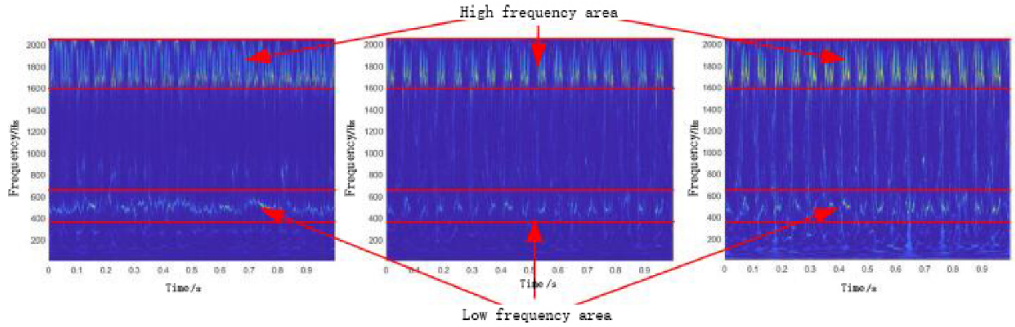

(a)Trouble-free vibration **(b)Anchoring eccentricity failure** **(c) Severe failure of broken teeth**

Figure 13. Comparison of the time–frequency vector of high- and low-frequency regions.

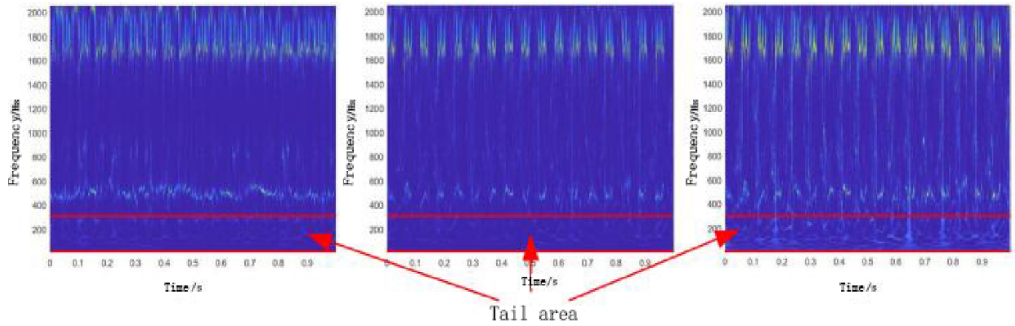

(a)Trouble-free vibration **(b)Anchoring eccentricity failure** **(c) Severe failure of broken teeth**

Figure 14. Time–frequency vector sweep area.

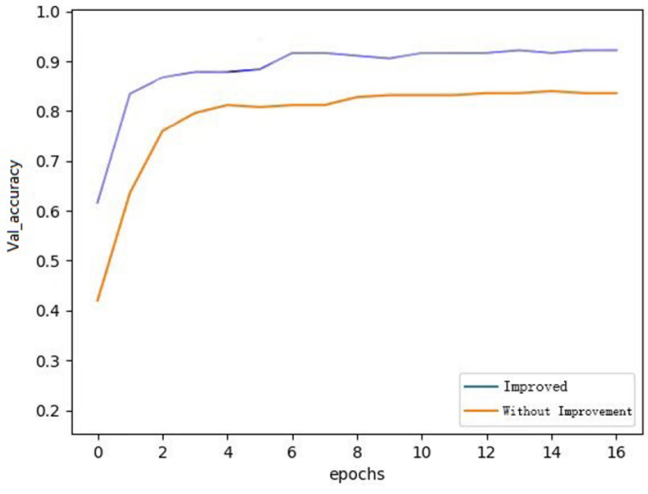

Figure 15. Comparison of recognition accuracy with and without improvement.

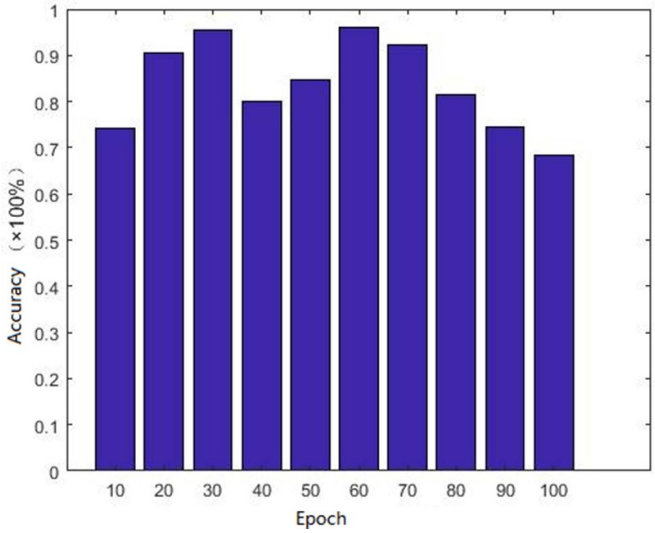

Figure 16. Graph of epoch versus recognition accuracy.

grasp the influence of the initial learning rate on the performance of the model, the epoch was set to 30 and the batch size to 30, and the learning rate was continuously changed. The obtained experimental results are shown in figure 17.

From the analysis of figure 17, we can see that the highest accuracy rate occurs when the learning rate is 0.0001. When the learning rate is greater than 0.0001 (between 0.001 and 0.18) the accuracy rate will decline, and when the learning rate is between 0.1 and 0.18 the accuracy rate drops to a lower level and remains unchanged at 33.33%. This is due to the fact that the learning rate increases and each training crosses the optimal region, making the overall performance of the model poorer. However, too slow a learning rate can also lead to a decrease in the accuracy of the model.

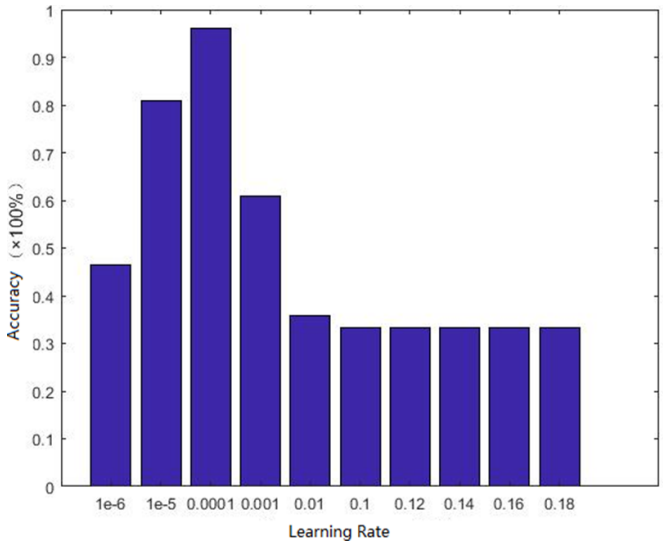

Figure 17. The relationship between learning rate and recognition accuracy.

Table 2. Improved model parameters.

Parameters	Value
Epoch	30
Learning rate	0.0001
Batch Size	30
Accuracy	96.14%
Memory consumption	14.45MB
No. of participants	720 000
Identification time	0.95 s

6.3.4. Complexity analysis of the improved model. In order to further analyze the performance of the improved model, the amount of memory occupied by the model, the number of parameters, the CPU recognition time and the GPU (NVIDIA RTX2080) recognition time were counted as further measures of model performance, combined with the above experiments. The parameters of the improved model are shown in table 2. As can be seen from the table, the number of parameters of the improved lightweight CNN model is only 720 000, and the accuracy rate can reach 96.14%. Compared with traditional CNN models, such as AlexNet, ResNet-18, VGG16, etc, which have tens or billions of parametric counts and a 100 trillion memory footprint, they are more lightweight. Currently, the storage system of the casing cutter can reach 128 MB after expansion. For the improved model, that occupies only 14.45 MB of memory, the storage system of the casing cutter fully meets the demand.

7. Conclusions

In order to obtain the vibration signal characteristics, a HT-VSA was designed, and a casing cutter measurement model was established, including the model of the casing cutter in a trouble-free state and two other common fault states. The vibration characteristics of the model were analyzed and the analysis results showed that environmental noise can cause the fault signature information to be drowned out. In order to solve the problem of overwhelming fault feature information, a fault feature enhancement model based on SNR enhancement and sparse representation was designed. The MobileNet-V3-Small CNN model was improved by reducing the basic blocks of the continuous homogeneous structure in the original model and expanding the SE structure to the global level to obtain a lightweight CNN fault recognition model. Various experiments have shown that the fault identification method can complete fault type identification more accurately.

Data availability statement

The data that support the findings of this study are available upon reasonable request from the authors.

Acknowledgments

This work was supported by Research Fund for the COSL Program (YJB19YF005) and CNOOC Program (JTKY-SXSH-2019-YF-01).

ORCID iDs

Pu Zhang https://orcid.org/0000-0002-5936-9211
Shuyao Liu https://orcid.org/0000-0002-3697-542X
Jingjing Cheng https://orcid.org/0000-0003-2857-9678

References

[1] Mohammed A I, Oyeneyin B, Atchison B and Njuguna J 2019 Casing structural integrity and failure modes in a range of well types—a review *J. Nat. Gas Sci. Eng.* **68** 102898
[2] Vrålstad T, Saasen A, Fjær E, Øia T, Ytrehus J D and Khalifeh M 2019 Plug and abandonment of offshore wells: ensuring long-term well integrity and cost-efficiency *J. Petrol. Sci. Eng.* **173** 478–91
[3] Kong D *et al* 2020 A BHA with integrated casing cutting and fishing tools applied in offshore of well abandonment *The 30th Int. Ocean and Polar Engineering Conf.* (International Society of Offshore and Polar Engineers)
[4] Khalifeh M and Saasen A 2020 Tools and techniques for plug and abandonment *Introduction to Permanent Plug and Abandonment of Wells* (Cham: Springer Open) pp 213–47
[5] Janssens O *et al* 2016 Convolutional neural network based fault detection for rotating machinery *J. Sound Vib.* **377** 331–45
[6] Suh S, Lee H, Jo J, Lukowicz P and Lee Y 2019 Generative oversampling method for imbalanced data on bearing fault detection and diagnosis *Appl. Sci.* **9** 746
[7] Li S, Liu G, Tang X, Lu J and Hu J 2017 An ensemble deep convolutional neural network model with improved DS evidence fusion for bearing fault diagnosis *Sensors* **17** 1729
[8] Osorio Santander E J, Silva Neto S F, Vaz L A and Monteiro U A 2020 Using spectral kurtosis for selection of the frequency bandwidth containing the fault signature in rolling bearings *Marine Syst. Ocean Technol.* **15** 243–52

[9] Hou G *et al* 2020 Bearing fault diagnosis based on variational mode decomposition and modified CNN *LSMS 2020 and ICSEE 2020 Workshops* (https://doi.org/10.1007/978-981-33-6378-6_16)
[10] Yan X, Liu Y, Xu Y and Jia M 2021 Multichannel fault diagnosis of wind turbine driving system using multivariate singular spectrum decomposition and improved Kolmogorov complexity *Renew. Energy* **170** 724–48
[11] Wang H *et al* 2021 Feature-level attention-guided multitask CNN for fault diagnosis and working conditions identification of rolling bearing *IEEE Trans. Neural Netw. Learn. Syst.* **1** 1–13
[12] Li X, Jiang H, Wang R and Niu M 2021 Rolling bearing fault diagnosis using optimal ensemble deep transfer network *Knowl.-Based Syst.* **213** 106695
[13] Aljemely A H, Xuan J, Jawad F K J, Al-Azzawi O and Alhumaima A S 2020 A novel unsupervised learning method for intelligent fault diagnosis of rolling element bearings based on deep functional auto-encoder *J. Mech. Sci. Technol.* **34** 4367–81
[14] Xiao S, Zhang F and Liang Z 2018 A mathematical casing cutting model and operation parameters optimization of a large-diameter deepwater hydraulic cutter *J. Petrol. Sci. Eng.* **162** 76–83
[15] Peng J, Cheng J, Wu L and Li Q 2020 Data acquisition and processing circuit for high-temperature logging up to 200 °C *Microelectron. Int.* **37** 131–8
[16] Postel M *et al* 2019 Monitoring of vibrations and cutting forces with spindle mounted vibration sensors *Manuf. Technol.* **68** 413–6
[17] Veronika K and Frank P 2018 A joint Tikhonov regularization and augmented lagrange approach for Ill-posed state constrained control problems with sparse controls *Numer. Funct. Anal. Optim.* **39** 1543–73
[18] Rudin L, Lions P L and Osher S 2003 *Multiplicative Denoising and Deblurring: Theory and Algorithms Geometric Level Set Methods in Imaging, Vision, and Graphics* (Berlin: Springer) pp 103–19
[19] Starck J L, Murtagh F and Fadili J M 2010 *Sparse Image and Signal Processing: Wavelets, Curvelets, Morphological Diversity* 1st edn (Cambridge: Cambridge University Press) (https://doi.org/10.1017/CBO9780511730344)
[20] Ophir B, Lustig M and Elad M 2011 Multi-scale dictionary learning using wavelets *IEEE J. Sel. Top. Signal Process.* **5** 1014–24
[21] Howard A *et al* 2019 Searching for mobilenetv3 *2019 Int. Conf. on Computer Vision (ICCV)* (*Seoul, Korea, 27 October–2 November 2019*) (Proceedings of the IEEE/CVF) pp 1314–24
[22] Gong D *et al* 2019 Memorizing normality to detect anomaly: memory-augmented deep autoencoder for unsupervised anomaly detection *2019 Int. Conf. on Computer Vision (ICCV)* (*Seoul, Korea, 27 October–2 November 2019*) (Proceedings of the IEEE/CVF) pp 1705–14
[23] Xia Y *et al* 2020 Synthesize then compare: detecting failures and anomalies for semantic segmentation *2020 European Conf. on Computer Vision (ECCV)* (*Glasgow,UK, 23–28 August 2020*) (Springer) pp 145–61
[24] Bergmann P *et al* 2020 Uninformed students: student–teacher anomaly detection with discriminative latent embeddings *2020 Conf. on Computer Vision and Pattern Recognition (CVPR)* (*Seattle, WA, USA, 13–19 June 2020*) (Proceedings of the IEEE/CVF) pp 4183–92
[25] Yi J and Yoon S 2020 Patch SVDD: patch-level SVDD for anomaly detection and segmentation *2020 Asian Conf. on Computer Vision (ACCV)* (*Kyoto, Japan, 30 November–4 December 2020*) (Springer) (https://doi.org/10.1007%2F978-3-030-69544-6_23)
[26] Kwon G *et al* 2020 Backpropagated gradient representations for anomaly detection *2020 European Conf. on Computer Vision (ECCV)* (*Glasgow, UK, 23–28 August 2020*) (Springer) pp 206–26